





Cite this: *Phys. Chem. Chem. Phys.*,  
2018, 20, 22537

## Defect generation in TiO<sub>2</sub> nanotube anodes via heat treatment in various atmospheres for lithium-ion batteries†

Andreas I. Savva, Kassiopiea A. Smith, Matthew Lawson, Sterling R. Croft, Ariel E. Weltner, Chris D. Jones, Hailey Bull, Paul J. Simmonds,  Lan Li and Hui Xiong \*

In this paper, ordered TiO<sub>2</sub> nanotubes were grown on a Ti substrate via electrochemical anodization and subsequently annealed at 450 °C for 4 h under various atmospheres to create different point defects. Oxygen-deficient environments such as Ar and N<sub>2</sub> were used to develop oxygen vacancies, while a water vapor (WV) atmosphere was used to generate titanium vacancies. Computational models by density functional theory predicted that the presence of oxygen vacancies would cause electronic conductivity to increase, while the presence of Ti vacancies could lead to decreased conductivity. The predictions were confirmed by two-point electrical conductivity measurements and Mott–Schottky analysis. Raman spectroscopy was also conducted to confirm the presence of defects. The annealed samples were then evaluated as anodes in lithium-ion batteries. The oxygen-deficient samples had an improvement in capacity by 10% and 25% for Ar- and N<sub>2</sub>-treated samples, respectively, while the WV-treated sample displayed a capacity increase of 24% compared to the stoichiometric control sample (annealed in O<sub>2</sub>). Electrochemical impedance spectroscopy studies revealed that the WV-treated sample's increased capacity was a consequence of its higher Li diffusivity. The results suggest that balanced electrical and ionic conductivity in nanostructured metal oxide anodes can be tuned through defect generation using heat treatments in various atmospheres for improved electrochemical properties.

Received 10th July 2018,  
Accepted 16th August 2018

DOI: 10.1039/c8cp04368j

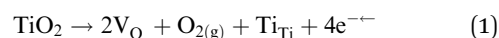
rs.c.li/pccp

## Introduction

There has been growing demand for improved performance in electrode materials for lithium-ion batteries as electric vehicles and electric grid storage become more prevalent. Graphite is commonly used as the anode in lithium-ion batteries and has a theoretical capacity of 372 mA h g<sup>-1</sup>.<sup>1–3</sup> Despite its widespread use, there are concerns about its safety and long-term stability as its lithiation potential (~0.1 V vs. Li/Li<sup>+</sup>) is close to that of lithium plating, which could lead to dendrite formation and short-circuiting.<sup>2,4</sup> Titanium dioxide (TiO<sub>2</sub>) is a promising alternative as it is cheap, environmentally friendly, abundant, and has comparable theoretical capacity with graphite (335 mA h g<sup>-1</sup>), along with a higher lithiation potential (~1.5–1.8 V vs. Li/Li<sup>+</sup>).<sup>2,5–9</sup> TiO<sub>2</sub> has multiple polymorphs (anatase, TiO<sub>2</sub>-B, rutile, brookite, etc.), and anatase TiO<sub>2</sub> is

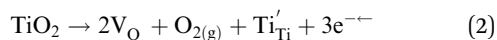
most commonly used in lithium-ion batteries, as its tetragonal structure has a high degree of octahedral sites for Li intercalation.<sup>4,7,10,11</sup> Yet in practice only 0.5 Li per Ti can intercalate in bulk anatase, resulting in a much lower capacity compared to its theoretical value. This is primarily due to its poor electrical conductivity and lithium diffusivity.<sup>1,2,6</sup> Nanostructured metal oxides can alleviate these issues, as they can shorten the distance that Li ions and electrons need to travel.<sup>1,2,5,6,8,12</sup>

The generation of point defects in TiO<sub>2</sub> and other metal oxides has been shown to improve their functionalities in a few applications. Through the introduction of defects, metal oxides have demonstrated superior properties for applications in photocatalysts, solar cells, and batteries.<sup>13–20</sup> These defects can be induced through methods such as substitutional doping or ion irradiation.<sup>21–25</sup> Another approach to create point defects is through annealing under different atmospheres.<sup>13,19,26–29</sup> If TiO<sub>2</sub> is annealed under oxygen-deficient environments (e.g., under pure Ar or N<sub>2</sub>), oxygen vacancies can form and generate free electrons, as well as reduce Ti (eqn (1) and (2))<sup>12,14,26–28</sup> and can be expressed in the classical Kröger–Vink notation as follows:



Micron School of Materials Science and Engineering, Boise State University,  
1910 University Drive, Boise, ID 83725, USA. E-mail: clairexiong@boisestate.edu;  
Tel: +1-208-426-5671

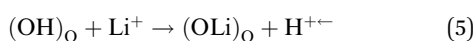
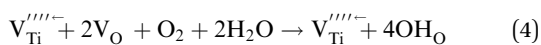
† Electronic supplementary information (ESI) available: Bode plots, XRD spectra, and first cycle dQ/dV plots of anatase TiO<sub>2</sub> nanotubes annealed under different atmospheres. See DOI: 10.1039/c8cp04368j



Oxygen vacancy formation may result in higher electronic conductivity, improved rate capability, and higher capacity.<sup>14,16,18,26,29,30</sup> Under heat treatments where oxygen is present, any oxygen vacancies already present in the sample will be eliminated, making  $\text{TiO}_2$  more stoichiometric (eqn (3)).



Cation vacancies may be stabilized if water vapor (WV) is added to an oxygen-rich annealing environment.<sup>31</sup> The water vapor may protonate existing oxygen sites and cause a positive charge, which would subsequently stabilize cation vacancies present in the sample (eqn (4)). It has been shown in  $\text{TiO}_2$  and other metal oxides that cation vacancies may provide more sites for lithium intercalation and therefore increase capacity.<sup>15,23,31–33</sup> Furthermore, during Li intercalation, the Li ions can exchange with protons without affecting the charge balance, which would provide additional sites to store Li, and thus also increase capacity (eqn (5)).<sup>31</sup>



Herein, we report a systematic investigation of anatase  $\text{TiO}_2$  nanotubes as an anode in lithium-ion batteries after they were subjected to different atmospheric heat treatments to generate point defects. Density functional theory (DFT) calculations were conducted to predict the effects that oxygen and cation vacancies would have on the electrical properties of  $\text{TiO}_2$  by creating theoretical band structures and partial charge models.  $\text{TiO}_2$  nanotube electrodes were prepared *via* electrochemical anodization and subsequently annealed under various atmospheres ( $\text{O}_2$ , Ar,  $\text{N}_2$ , and WV). The nanotube thin film samples were subjected to two-point conductivity measurements and Mott–Schottky analysis to determine how each annealing condition affected the electrical conductivity of the nanotubes. Raman spectroscopy was used to confirm the presence of the various point defects, while X-ray diffraction (XRD) and scanning electron microscopy (SEM) were used to observe any crystallographic or morphological changes in the nanotubes as a consequence of the heat treatments. Electrochemical testing was also conducted to elucidate how the resulting point defects improved battery performance. The characterizations and testing revealed that the Ar and  $\text{N}_2$  treatments increased the electrical conductivity of the samples due to oxygen vacancy formation, while the WV treatment created Ti vacancies which lowered the electrical conductivity. Nevertheless, both the  $\text{N}_2$ - and WV-treated samples exhibited the largest specific capacity increase among tested samples. In addition, the  $\text{N}_2$ -treated samples had the best rate capability, while the WV-treated samples had the largest Li diffusivity. Our results suggested that both electronic conductivity and ionic conductivity in intercalation electrode materials need to be considered for understanding their charge storage and transport properties, and the type of defects has a critical influence on the charge storage and transport mechanism in metal oxide electrodes.

## Methods

### Anodization of Ti foil

Ti foil (Alfa Aesar, 0.032 mm thick) was cut into 4 × 4.5 cm pieces and sonicated in acetone, isopropanol, and DI water for 5 minutes each. The foil was then air-dried and had its back protected with acrylic sheeting and packing tape for uniform current distribution during anodization. The prepared foil was anodized in a solution of 0.27 M  $\text{NH}_4\text{F}$  in formamide, with Pt mesh as the counter electrode, for 30 minutes at 15 V and 0.2 A. After anodization was complete, the foil was dipped in DI water to remove excess solution and then sonicated in isopropanol and DI water for three 1-second bursts each. The foil then had its backing carefully peeled off and was put to dry for several hours in a vacuum oven at approximately 70 °C.

### Annealing of $\text{TiO}_2$ nanotubes

Four 15 mm discs were punched out of each sample using a Precision Disk Cutter (MTI). One disc from each sample was sacrificed for active weight measurements by using scotch tape to strip the nanotubes from the Ti substrate. The other three discs were annealed in an OTF-200X tube furnace (MTI) at 450 °C for 4 h under  $\text{O}_2$  (80% Ar, 20%  $\text{O}_2$ ), Ar (99.9%),  $\text{N}_2$  (99.9%), and water vapor (80% Ar, 20%  $\text{O}_2$ ). The WV atmosphere was generated by bubbling  $\text{O}_2$  gas (80% Ar, 20%  $\text{O}_2$ ) through a water bath heated to 80 °C. The gas flow rate was held constant (one bubble per second) with minimal variation between atmospheric treatments.

### Electrochemical measurements

Coin cells (Hohsen 2032) were assembled in an Ar-filled glovebox (Mbraun) with an  $\text{O}_2$  concentration less than 0.5 ppm. The annealed  $\text{TiO}_2$  discs were the working electrodes and Li metal (FMC lithium) was used as the counter electrode with microporous polyolefin separators (Celgard 2325). The electrolyte was 1.2 M  $\text{LiPF}_6$  (Tomiyama) in ethylene carbonate/ethyl methyl carbonate (3 : 7 weight ratio). The cells were then cycled from 0.9 to 2.5 V vs.  $\text{Li}/\text{Li}^+$  at a theoretical C rate of C/20 (16.75 mA  $\text{g}^{-1}$ ) using an automated battery tester (Arbin). For the rate study, the cells were cycled in the same voltage window at theoretical C rates of C/20, C/10, C/5, C/2, 1C, and 5C. The cells were placed in a ThermoFisher Heratherm incubator during cycling at a constant temperature of 25 °C.

Mott–Schottky analysis was performed using the SPEIS program on a Bio-Logic VMP-300 in a three-electrode cell. Samples were masked with Kapton tape with a 15 mm diameter area left exposed. A Pt mesh was used as the counter electrode in an aqueous 1 M KOH solution. A Ag/AgCl reference electrode was used. Samples were subsequently analyzed in a frequency range from 100 kHz to 100 mHz with an excitation voltage of 10 mV from 0.1 to −1 V vs. Ag/AgCl in 0.05 V increments. Electrochemical impedance spectroscopy (EIS) was done on a Bio-Logic VMP-300 using a three-electrode cell (EL-CELL). Samples were analyzed in a frequency range from 100 kHz to 5 mHz at open circuit voltages by applying a sinusoidal voltage with an amplitude of 5 mV.

## Characterizations

XRD was done using a Rigaku MiniFlex 600 with a 600 W generator and Cu target;  $2\theta$  was scanned from 20–85°. The instrumental broadening was accounted for by scanning a LaB<sub>6</sub> standard and subtracting the peak width from the resulting experimental data. The nanotube morphology was observed *via* SEM using a FEI Teneo field emission microscope operating at 5 kV. Raman spectroscopy was completed with a Horiba Scientific LabRam HR Evolution spectrometer using a 442 nm He:Cd laser with signal accumulation of 30 s scans. After instrument calibration, the samples were scanned at room temperature with an incident laser power of 100 mW from 100–1000 cm<sup>-1</sup>. Samples were viewed at a magnification of 100× and scattered light was collected with a thermoelectrically cooled Si CCD detector.

Two-point electrical conductivity measurements were used to determine the out-of-plane conductivity of the nanotubes. A silver paint contact was placed on the nanotube surface with another on the back of the Ti foil; copper wire was attached to the bottom to serve as a contact point for the instrument. The contacts were about 2 mm in diameter and a current of 10 μA was applied to each sample. A porosity of 0.46 was used to calculate the electrical conductivity (ESI<sup>†</sup>). A Keithley 237 High Voltage Source Measure Kit was used to apply the current to each sample and a Keithley 2000 Multimeter was used to record the resulting resistance.

## Computational modeling

To predict the electronic structure and properties of the anatase TiO<sub>2</sub>, density functional theory (DFT) was performed using VASP.<sup>34</sup> The exchange–correlation energies were described using the PBE (Perdew–Burke–Ernzerhof) pseudopotentials and GGA (Generalized Gradient Approximation).<sup>35</sup> A cut-off energy of 380 eV was chosen to account for the plane-wave basis set. To incorporate a rich electronic structure, the unit cell of the anatase phase was expanded into a 3 × 3 × 1 supercell with a  $\Gamma$ -centered 5 × 5 × 7  $k$ -point mesh sampling in the Brillouin zone.

The electronic structures and properties of pristine, oxygen-deficient, and Ti-deficient anatase TiO<sub>2</sub> were calculated from their respective ground state structures with residual forces of

0.1 eV Å<sup>-1</sup> and an electronic convergence of 1 × 10<sup>-6</sup> eV. The band structures of these systems were also determined. To account for the strongly correlated d orbital effect on titanium, the DFT+*U* scheme was applied with an on-site Coulomb potential of 8.0 eV, and the partial charge densities were also generated 2 eV above and below the Fermi energy to further study how the electron density distribution was affected by various defects.<sup>36</sup>

## Results and discussion

Computational modeling was conducted to predict the electronic properties of anatase TiO<sub>2</sub> and the effects of oxygen and titanium vacancies. For the pristine anatase structure, the bandgap was found to be approximately 3.2 eV, agreeing well with literature reported values *via* experiments and theoretical calculations (Fig. 1a).<sup>37–41</sup> There were significant changes to the band structure after an oxygen atom was removed from the anatase supercell, which resulted in an oxygen vacancy concentration of 1.39%. The Fermi energy shifted into the conduction band (*viz.*, the conduction band shifted below the Fermi energy), and a mid-gap state appeared about 0.8 eV below the conduction band (Fig. 1b). The Fermi energy shift and the development of a mid-gap state were expected, as previous experimental studies had shown similar results.<sup>39,42,43</sup> The new mid-gap state is indicative of Ti<sup>3+</sup> defect states, which have developed due to the introduction of oxygen vacancies, and subsequently act as electron donors for n-type semiconducting characteristics.<sup>38,43</sup> These changes could potentially cause an increase in the electrical conductivity for the oxygen-deficient case due to n-type semiconductor behavior.

Since our computational model was in agreement with literature for the oxygen-deficient structure, the same approach was used for the Ti vacancy scenario. 4H<sup>+</sup> ions were inserted into the O sites around the vacancy to stabilize it and more accurately represent the defects introduced during WV treatment. A defect concentration of 2.77% was achieved upon the removal of a Ti atom from the supercell.

The resulting band structure changes for Ti-deficient anatase were not as drastic compared to the introduction of

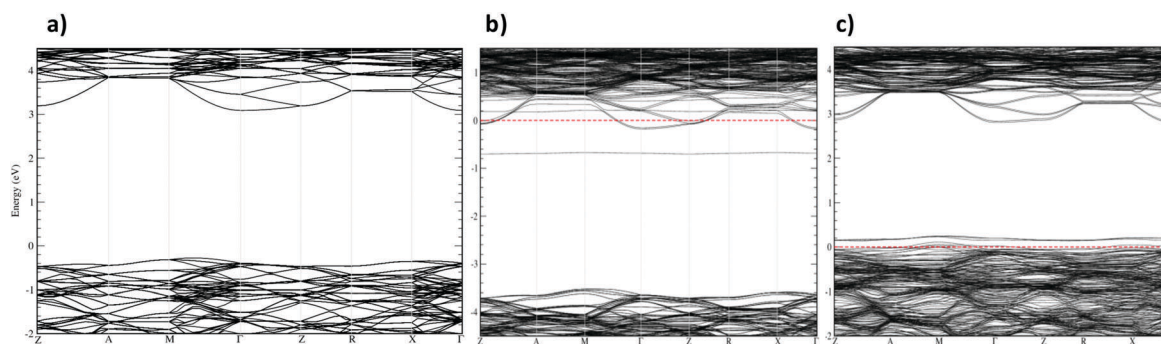


Fig. 1 Theoretical band structures of (a) pristine anatase TiO<sub>2</sub>, (b) anatase TiO<sub>2</sub> with O vacancy, and (c) anatase TiO<sub>2</sub> with Ti vacancy stabilized with 4 protonated O sites. Red line indicates the Fermi energy.

an oxygen vacancy, but they were still significant. The Fermi energy shifted down into the valence band (*viz.*, the valence band shifted above the Fermi energy) and a new band appeared less than 0.2 eV above the valence band (Fig. 1c). These changes imply that a large concentration of Ti vacancies in TiO<sub>2</sub> may result in p-type semiconductor behavior. However, it was unclear from this result whether the oxygen or Ti vacancies would have a larger impact on the electrical conductivity.

In order to further investigate the defect influence on the electronic properties, partial charge density (*i.e.*, band decomposed) calculations were conducted for the valence band maximum (VBM) and conduction band minimum (CBM) states, as shown in Fig. 2. The figure depicts available charge states for a given energy range. The energy range from -2.0 eV to 0 eV was used for the VBM, while 0 eV to 2.0 eV was used for the CBM. In comparison to pristine anatase TiO<sub>2</sub> (Fig. 2a), the partial charge density with the O vacancy at the VBM is highly localized around the vacancy site (Fig. 2b). Fig. 2c shows that the partial charge density with the Ti vacancy at the VBM decreases at the O sites but they remain at the Ti sites. In addition, the CBM analysis indicates that the partial charge density with the O vacancy is more localized both at the Ti and O sites in Fig. 2e than that for pristine anatase TiO<sub>2</sub> (Fig. 2d) and the Ti vacancy case (Fig. 2f). The computational results suggest that the oxygen vacancy could potentially cause an increase in electrical conductivity while the Ti vacancy would decrease it.

To validate these predictions, TiO<sub>2</sub> nanotubes were annealed under O<sub>2</sub>, Ar, N<sub>2</sub>, and WV at 450 °C for 4 h to generate the appropriate defects. The samples were then characterized to determine whether the electrical properties had been altered as a result of the various atmospheric heat treatments. Mott-Schottky characterizations enabled the quantitative

measurement of the samples' charge carrier densities. It is important that the appropriate frequency was selected for analysis of Mott-Schottky tests. The charge carrier density of the sample was determined from space charge capacitance ( $C_{sc}$ ), which was obtained from  $Z''$ , the imaginary contribution to impedance and the frequency  $f$  (eqn (6)).<sup>44,45</sup>

$$C_{sc} = -\frac{1}{2\pi f Z''} \quad (6)$$

If the frequency was too low, surface state capacitance ( $C_{ss}$ ) would contribute to the total capacitance, incorrectly shifting results towards higher carrier density values.<sup>44</sup> In addition, the real contribution to impedance,  $Z'$ , would also vary with frequency.<sup>44</sup> As a consequence, Bode plots in the frequency range of 100 kHz–100 mHz were used to determine the frequency at which  $Z''$  becomes constant (ESI<sup>†</sup>). The plot for each atmosphere indicated that  $Z''$  plateaus at a frequency of about 500 Hz; the curves at 1.3 kHz were therefore used to calculate the charge carrier density for each sample. The following equation (eqn (7)) relates the charge carrier density to the capacitance of the Mott-Schottky plot, where  $q$  is the charge of an electron,  $\epsilon$  is the dielectric constant (31 for anatase),<sup>27,46</sup>  $\epsilon_0$  is the vacuum permittivity constant,  $N_D$  is the charge carrier density,  $A$  is the geometric surface area,  $V_{fb}$  is the flat-band potential,  $V$  is the applied potential,  $k$  is Boltzmann's constant, and  $T$  is the temperature.<sup>45,47</sup>

$$C_{sc}^{-2} = \left( \frac{2}{q\epsilon\epsilon_0 N_D A^2} \right) \left( V - V_{fb} - \frac{kT}{q} \right) \quad (7)$$

Eqn (8) is then differentiated with respect to the voltage and manipulated to the below form (eqn (8)) where the slope of

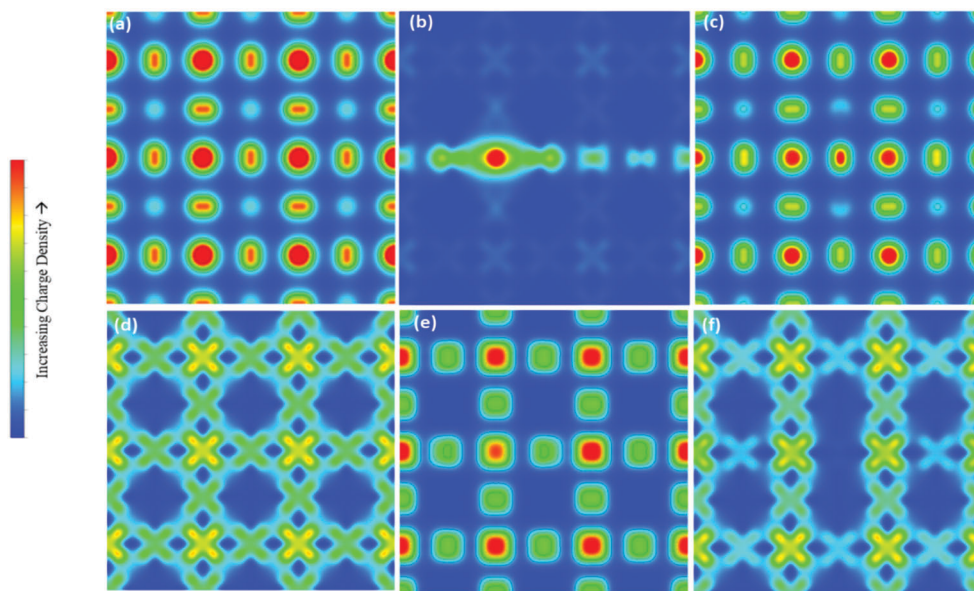


Fig. 2 Partial charge density calculations for pristine anatase TiO<sub>2</sub> (a and d), anatase TiO<sub>2</sub> with O vacancy (b and e), anatase TiO<sub>2</sub> with Ti vacancy (c and f). Images (a–c) refer to the valence bands, (d–f) are the conduction bands. 2D images projected along the *c* axis.



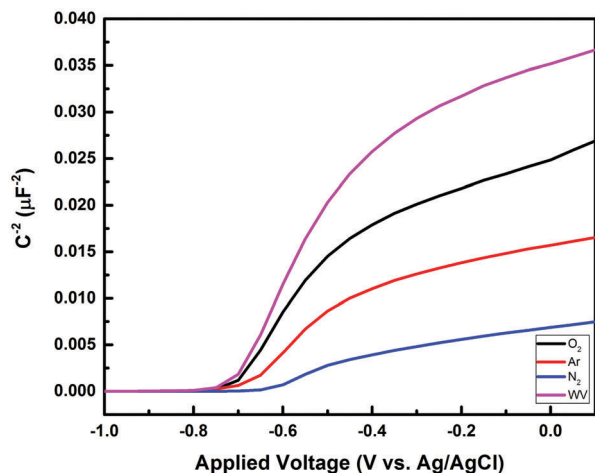


Fig. 3 Mott-Schottky plots at 1.3 kHz of anatase TiO<sub>2</sub> nanotubes annealed under different atmospheres.

the plot's linear region  $\frac{dC^{-2}}{dV}$  is used to obtain the charge carrier density.

$$N_D = \frac{2}{q\epsilon\epsilon_0 A^2} \left( \frac{dC^{-2}}{dV} \right)^{-1} \quad (8)$$

Each Mott-Schottky curve (Fig. 3) had a positively sloped linear region, confirming the n-type semiconductor behavior expected for TiO<sub>2</sub>.<sup>45,47-50</sup> According to eqn (8), as the slopes become less steep, the charge carrier densities will increase. From the Mott-Schottky plot, the O<sub>2</sub> and WV samples have the lowest carrier densities, followed by Ar and N<sub>2</sub> (Table 1). These results corroborate well with the computational models. Annealing under oxygen-deficient conditions should result in the generation of oxygen vacancies, which would result in the presence of more free electrons in the TiO<sub>2</sub> nanotube structure. Since TiO<sub>2</sub> is a n-type semiconductor, its charge carriers are electrons, which means an increase in electrons would lead to a shallower slope in the Mott-Schottky plots. The slight positive shift of the flat-band potential for the oxygen-deficient treatments also suggests that oxygen vacancies may have formed.<sup>13,50</sup> The WV sample has a small decrease in charge carrier density compared to the O<sub>2</sub> control at 1.3 kHz, which is also consistent with results from the simulations.

Electrical conductivity measurements were subsequently done to compare with the conclusions drawn from the Mott-Schottky analysis. Using a two-point measurement,<sup>48</sup> the out-of-plane conductivities of the annealed nanotubes were

Table 1 Charge carrier densities and flat-band potentials of anatase TiO<sub>2</sub> nanotubes annealed under different atmospheres

Atmosphere	Charge carrier density (cm <sup>-3</sup> )	Flat-band potential (V)
O <sub>2</sub>	2.01 × 10 <sup>19</sup>	-0.715
Ar	3.31 × 10 <sup>19</sup>	-0.688
N <sub>2</sub>	8.06 × 10 <sup>19</sup>	-0.650
WV	1.49 × 10 <sup>19</sup>	-0.716

Table 2 Electrical conductivity of TiO<sub>2</sub> nanotubes annealed under different atmospheres

Atmosphere	Electrical conductivity (S m <sup>-1</sup> )
O <sub>2</sub>	3.28 × 10 <sup>-2</sup>
Ar	6.86 × 10 <sup>-2</sup>
N <sub>2</sub>	1.41 × 10 <sup>-3</sup>
WV	6.33 × 10 <sup>-3</sup>

found (Table 2). The oxygen-deficient atmospheres increased electrical conductivity, with the N<sub>2</sub> treatment changing by two orders of magnitude. In contrast, the WV treatment caused the electrical conductivity to decrease. These results were consistent with the Mott-Schottky data, as changes in charge carrier density should correlate with the electrical conductivity.

Our conductivities were also comparable with previously reported two-point measurements on anatase TiO<sub>2</sub> nanotubes.<sup>26,51</sup> The conductivity measurements and Mott-Schottky analysis corroborate well with the theoretical models. The Ar and N<sub>2</sub> treatments increase the electrical conductivity and charge carrier density of the anatase TiO<sub>2</sub> nanotubes, suggesting that the oxygen-deficient atmospheric annealing treatments have indeed created oxygen vacancies. On the other hand, the WV treatment displays a slight decrease in its electrical conductivity, which implies that Ti vacancies may have formed.

It is interesting to note that the Ar-treated samples have lower conductivities and carrier densities compared to the N<sub>2</sub>-treated samples. Although it is beyond the scope of this paper, the variation in conductivity as a result of the two different oxygen-deficient treatments may be due to their reactivity. Since Ar is a noble gas, it will not interact with any oxygen atoms that have been released from TiO<sub>2</sub>. Any oxygen atoms that do not combine to form O<sub>2</sub> will likely re-enter the TiO<sub>2</sub> structure. However, N<sub>2</sub> could form a variety of nitrogen oxides with the outgassed oxygen atoms, especially given the high annealing temperature. The consumption of additional oxygen atoms as a consequence of nitrogen oxide formation could explain the increase in oxygen vacancies and conductivity. Further research would have to be conducted to verify this proposed mechanism.

Additional characterizations were used to determine the morphological and crystallographic effects of the atmospheric heat treatments, as well as to further confirm the presence of the generated point defects. SEM images of the TiO<sub>2</sub> nanotubes after treatment show that the nanotubes maintain their structural integrity regardless of annealing conditions, with an average outer tube diameter of approximately 60–65 nm and tube wall thickness of about 10 nm (Fig. 4). Each of the annealed samples was subsequently characterized using XRD. As expected, the resulting XRD spectra for each sample matched well with anatase TiO<sub>2</sub> (ESI<sup>†</sup>). Strong Ti peaks were also present due to the Ti substrate.

In addition, there was a slight presence of rutile(110) peak in the XRD of the O<sub>2</sub> and WV samples, but not so much in the N<sub>2</sub> or Ar samples, which is consistent with previous reports on the inhibition of anatase-rutile transformation in

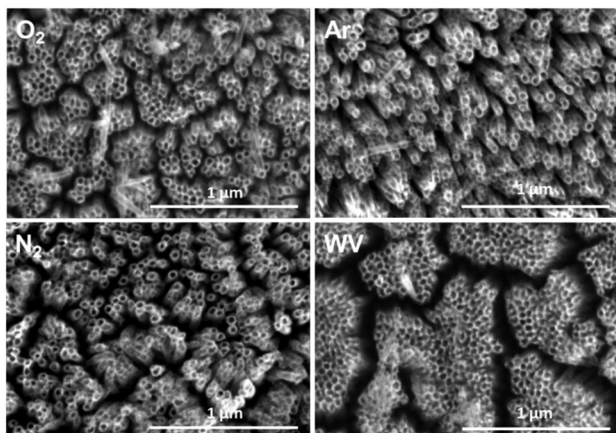


Fig. 4 SEM images of anatase TiO<sub>2</sub> nanotubes annealed under different atmospheres.

oxygen-deficient environments.<sup>17,20,24,50</sup> The weight percentage of the rutile phase was found using the equation developed by Spurr *et al.*<sup>52</sup> to be 16%, 9%, and 6% for the O<sub>2</sub>, WV-, and N<sub>2</sub>-treated samples, respectively, while there was no rutile phase present in the Ar-treated sample. The presence of rutile is likely concentrated primarily in the barrier layer between the nanotubes and the Ti substrate as reported previously.<sup>53</sup> However, it is unlikely that the rutile phase has a significant effect on the electrical conductivity of the samples treated by different atmospheres during annealing. While rutile has a higher electrical conductivity<sup>54</sup> compared to anatase due to a smaller band gap (3.0 eV in rutile *vs.* 3.2 eV in anatase), the percentage of rutile does not match the conductivity trend obtained from the two-point measurements. Furthermore, the charge carrier densities, which were obtained *via* Mott-Schottky analysis, only match the electrical conductivity trend and not the trend of rutile composition of the samples. This is significant as Mott-Schottky analysis is a surface technique, which indicates that the electrical conductivity trends are more reflective of the composition of the tubes at the surface (*viz.*, anatase TiO<sub>2</sub>) than the composition at the nanotube-substrate interface. Thus, the presence of rutile in the barrier layer has a negligible effect on the electrical properties of the anatase TiO<sub>2</sub> nanotubes.

Upon refining the XRD spectra, there were no significant changes in the unit cell parameters for samples annealed in different atmospheres compared to the O<sub>2</sub> control sample. This indicates that the changes in unit cell for the TiO<sub>2</sub> nanotubes as a consequence of the various heat treatments were negligible.

The annealed samples were also characterized using Raman spectroscopy (Fig. 5). Each sample clearly had the associated spectrum for anatase TiO<sub>2</sub>, with peaks present at approximately 144 cm<sup>-1</sup>, 395 cm<sup>-1</sup>, 517 cm<sup>-1</sup>, and 636 cm<sup>-1</sup>. These peaks correspond to the E<sub>g</sub>(1), B<sub>1g</sub>(1), B<sub>1g</sub>(2) + A<sub>1g</sub>, and E<sub>g</sub>(3) vibrational modes, respectively.<sup>26,55–57</sup> A small peak at 196 cm<sup>-1</sup> associated with the E<sub>g</sub>(2) vibrational mode was also present in all four samples.<sup>55,57</sup> As seen in Fig. 5, there are some differences in the annealed samples compared to the O<sub>2</sub> control sample.

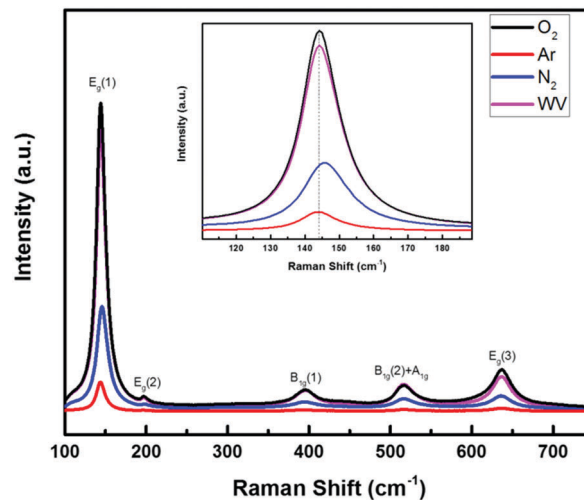


Fig. 5 Raman spectroscopy of anatase TiO<sub>2</sub> nanotubes annealed under different atmospheres. Inset: Enlarged region near E<sub>g</sub>(1) peak.

The N<sub>2</sub> sample has a slight blueshift of the E<sub>g</sub>(1) peak of about 1.77 cm<sup>-1</sup>, in addition to some peak broadening of about 1.32 cm<sup>-1</sup>. Strain, phonon confinement, and nonstoichiometry could all contribute to the development of the observed blueshift and broadening.<sup>56–61</sup> Williamson–Hall plots were used to determine whether strain was present in the samples; it was found that the strain was insignificant and thus did not contribute to the Raman peak shift (ESI<sup>†</sup>). Dispersion caused by phonons will occur if the crystallite size is small enough (*viz.*, less than 10–20 nm).<sup>26,30,56</sup> Using the Scherrer equation,<sup>62</sup> the crystallite size for the N<sub>2</sub> sample was found to be 48 nm. Since this value is larger than the critical limit of 20 nm, the broadening and shift of the E<sub>g</sub>(1) mode is not a consequence of phonon confinement. Thus, it is most probable that the observed changes in the E<sub>g</sub>(1) mode are due to the formation and proliferation of oxygen vacancies. Similar results have been reported in a number of studies on non-stoichiometric TiO<sub>2</sub> nanostructures.<sup>26,30,61,63</sup> Furthermore, the observed Raman shift for the N<sub>2</sub> sample is also in agreement with the computational models and enhanced electrical conductivity.

The other peaks of the N<sub>2</sub> sample are not shifted or broadened to any significant extent. The samples annealed under Ar and WV have negligible peak shift and broadening for all vibrational modes. This is expected for the WV sample, as no oxygen vacancies are expected to form. It also suggests that the Ti vacancy concentration is not large enough to have an effect on the Raman spectrum of anatase TiO<sub>2</sub>. The lack of peak shift is slightly surprising in the case of Ar, as it is also an oxygen-deficient atmosphere. However, the lower concentration of O vacancies for the Ar-treated sample may be responsible for the lack of E<sub>g</sub>(1) blueshift; this result is also consistent with the conductivity and Mott-Schottky measurements. In addition, other literature has shown that similar oxygen-deficient heat treatments can have significant variation in the degree of peak shift.<sup>26,30</sup> It should be noted that the N<sub>2</sub> and Ar samples have lower peak intensities compared to the O<sub>2</sub> and WV samples, as

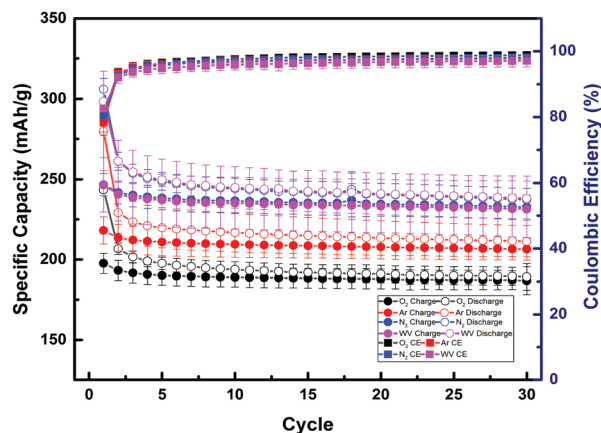


Fig. 6 Specific capacities of anatase  $\text{TiO}_2$  nanotube electrodes annealed under different atmospheres. Cells were cycled from 0.9 to 2.5 V at a theoretical C rate of C/20.

this decrease in intensity could indicate some disorder due to defect generation.

The annealed samples were subsequently used as anodes in lithium-ion batteries to determine their electrochemical performance. The  $\text{O}_2$ -treated control sample displayed an initial charge of  $197.6 \text{ mA h g}^{-1}$ , which stabilized to  $186.9 \text{ mA h g}^{-1}$  at C/20 after 30 cycles (Fig. 6). The capacity of the control sample was consistent with previously reported values for anatase  $\text{TiO}_2$  nanotubes in Li-ion systems.<sup>10,64,65</sup> There was a marked increase in specific capacity when the electrode was annealed in oxygen-deficient environments. The initial charge capacity for the Ar-treated sample was  $218.0 \text{ mA h g}^{-1}$  which decreased to  $206.4 \text{ mA h g}^{-1}$  after 30 cycles, while the  $\text{N}_2$ -treated sample had initial charge capacity of  $246.6 \text{ mA h g}^{-1}$  and dropped to  $232.7 \text{ mA h g}^{-1}$  after 30 cycles. The WV-treated sample exhibited a similar increase in capacity to the  $\text{N}_2$  sample. The initial charge capacity was  $246.5 \text{ mA h g}^{-1}$  and maintained  $231.3 \text{ mA h g}^{-1}$  after 30 cycles. The Coulombic efficiency after 30 cycles for all atmospheric treatments was fairly consistent, as the values for  $\text{O}_2$  control, Ar,  $\text{N}_2$ , and WV were 98.8, 97.7, 98.1, and 97.1%, respectively.

The changes in specific capacity as a consequence of atmospheric heat treatment were consistent with the aforementioned characterizations. These changes did not match with the percentage of rutile determined from the XRD patterns, confirming that the rutile phase had negligible impact on the nanotubes' electrochemical behavior. More significantly, the improved electrical conductivity displayed by the nanotubes due to the generation of oxygen vacancies in the Ar- and  $\text{N}_2$ -treated samples facilitated an increase in specific capacity. The disparity between the Ar- and  $\text{N}_2$ -treated samples is still present, as the  $\text{N}_2$  treatment has a significantly higher capacity compared to the Ar-treated sample. This difference is consistent with the electrical conductivity measurements and gives additional support to the claim that annealing under Ar generates fewer oxygen vacancies compared to  $\text{N}_2$ . It is important to note that the WV treatment resulted in capacity comparable to the  $\text{N}_2$  treatment, which suggests that the slight decrease in electrical

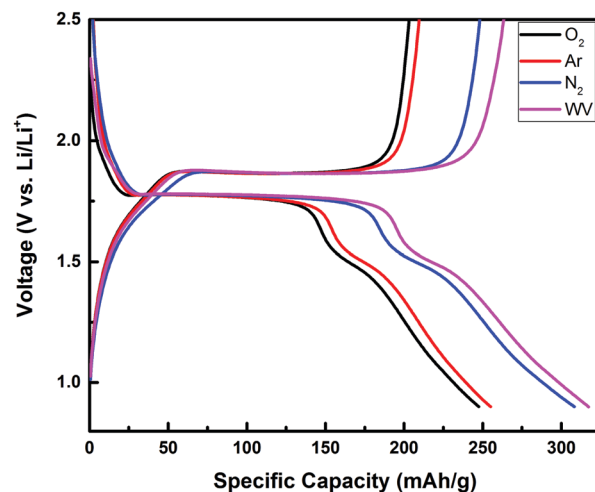


Fig. 7 1st cycle voltage profiles of anatase  $\text{TiO}_2$  nanotube electrodes annealed under different atmospheres. Cells were cycled at a theoretical C rate of C/20.

conductivity has a negligible effect on the anode's charge storage properties and the effect of the Ti vacancies on increased charge storage sites is more significant.

The voltage profiles of each sample were studied to determine whether there were any fundamental differences in electrochemical behavior (Fig. 7). The shape of the voltage profiles and  $dQ/dV$  plots (ESI<sup>†</sup>) were quite similar for each of the annealed samples. For all samples, a wide discharge two-phase plateau begins at about 1.78 V, which is followed by a much smaller plateau at approximately 1.5 V. The charge profile displays a change of slope near 1.6 V and its wide two-phase plateau region begins at approximately 1.87 V. The plateau regions for the charge and discharge profiles are consistent with the Li deintercalation and intercalation potentials for anatase  $\text{TiO}_2$ .<sup>8,10,64,66,67</sup> The presence of these plateaus indicates the addition and removal of Li ions to and from the octahedral interstitial sites.<sup>8,64,67</sup> The onset of the wide discharge plateau at 1.78 V corresponds to the transition of Li-poor anatase  $\text{TiO}_2$  to  $\text{Li}_{0.5}\text{TiO}_2$  (*Imma*) and the following plateau at 1.5 V then describes the transition of  $\text{Li}_{0.5}\text{TiO}_2$  to  $\text{LiTiO}_2$  (*I4<sub>1</sub>/amd*) with further lithium intercalation.<sup>68–70</sup> From the voltage profiles, it is apparent that the broadening of the anatase intercalation plateaus is responsible for the increase in capacity for the oxygen-deficient and WV atmospheres. The  $dQ/dV$  plots also correspond well to the voltage profiles (ESI<sup>†</sup>). One peak during charging was located at about 1.9 V with a faint peak around 1.7 V, while two peaks were located at 1.5 and 1.75 V during discharge.

Further characterizations were conducted to investigate the contradictory trends presented by the electrical conductivity measurements and electrochemical performance for the WV-treated sample. As a consequence, EIS was conducted to measure the Li diffusivity of the annealed samples (Fig. 8a). The equivalent circuit shown in Fig. 8b was fit to the experimentally obtained data to obtain the Li diffusivity (Table 3). The calculated diffusivities were comparable to values already reported in

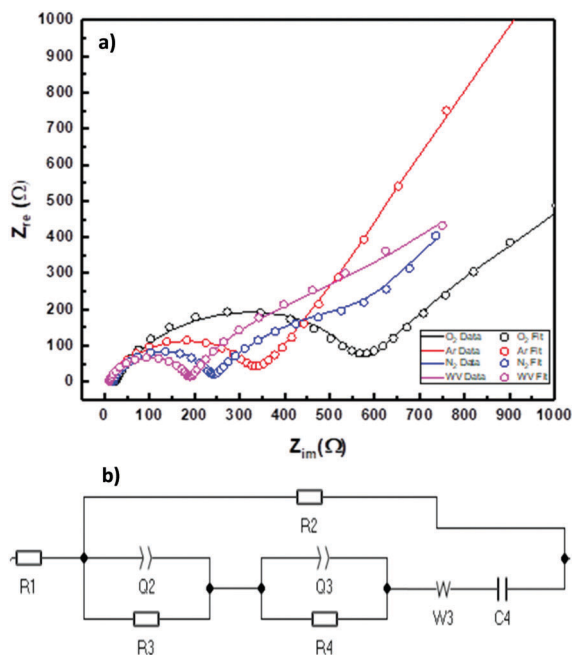


Fig. 8 (a) Nyquist plots of anatase TiO<sub>2</sub> nanotubes annealed under different atmospheres. (b) Equivalent circuit used to fit impedance data.

literature.<sup>71–73</sup> A term accounting for possible parasitic side reactions (R2) was included in the equivalent circuit to fit more closely with the experimental data, as the tested materials were uncycled and thus more sensitive to degradation.<sup>74</sup> From the fitting, it was found that the WV-treated sample had the largest Li diffusivity. The improvement of the Li diffusivity was particularly significant, as it was two orders of magnitude larger than the diffusivity of the O<sub>2</sub> control sample. The increased Li diffusivity helps justify the high specific capacity exhibited by the WV-treated sample. While Ti vacancies stabilized by the WV treatment decreased electrical conductivity, their presence facilitated Li ion diffusion.

Rate capability studies were also conducted to determine how the formation of the oxygen and Ti vacancies would affect the electrochemical performance of the TiO<sub>2</sub> nanotubes at elevated current rates (Fig. 9). At C/20, the charge capacities for the N<sub>2</sub>- and WV-treated samples were almost identical at 231.9 and 230.6 mA h g<sup>-1</sup>, respectively. However, the performance began to change as the C rate was increased. At C/2, their behavior noticeably differs, as the N<sub>2</sub>-treated sample had a charge capacity of 176.9 mA h g<sup>-1</sup>, while the WV treatment had a lower capacity of 166.0 mA h g<sup>-1</sup>. The most dramatic decrease in capacity occurred at the highest current rate of 5C. The N<sub>2</sub>

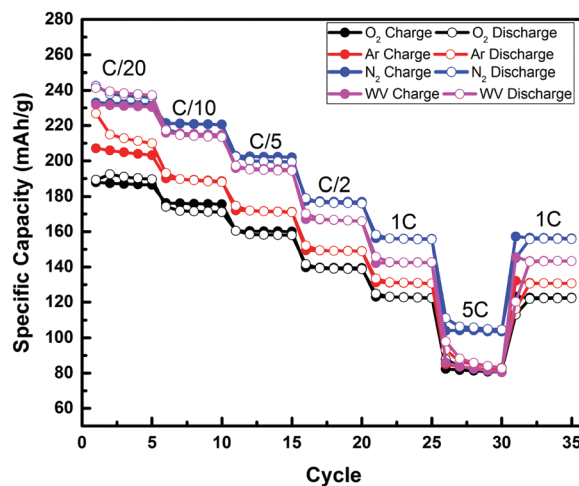


Fig. 9 Rate study of anatase TiO<sub>2</sub> nanotube electrodes annealed under different atmospheres.

treatment caused capacity to decrease to 103.5 mA h g<sup>-1</sup>, but the WV-treated sample had its capacity drop sharply to 80.4 mA h g<sup>-1</sup>, which was comparable to the O<sub>2</sub> control capacity of 80.5 mA h g<sup>-1</sup>. The Ar-treated sample maintained its slightly higher capacity with respect to the control case at all C rates until 5C. All samples exhibited good capacity recovery after being subjected to the highest current rate. The results of the rate study suggest that the electrical conductivity of the samples plays a larger role in their performance at higher rates. The higher Li diffusivity in the WV-treated sample does not enable it to perform well at higher C rates, but the N<sub>2</sub>-treated sample has adequate capacity at rates up to 5C. This indicates that a synergistic effect from both electronic and ionic conductivity is necessary to achieve high rate capability in intercalation oxide electrodes.

## Conclusions

Oxygen and titanium vacancies can be generated in TiO<sub>2</sub> nanotubes by annealing under oxygen-deficient (Ar and N<sub>2</sub>) and WV atmospheres, respectively. Oxygen vacancies cause the electrical conductivity of the samples to increase, while Ti vacancies result in a slight decrease of electrical conductivity as predicted by DFT calculations and evaluated through two-point electrical conductivity measurements and Mott–Schottky analysis. The formation of these defects was confirmed by Raman spectroscopy. Both kinds of defects result in an improvement in the specific capacity of the TiO<sub>2</sub> nanotubes when they are used as anodes in a Li-ion battery. The Ar- and N<sub>2</sub>-treated samples have an increase in capacity by 10% and 25%, respectively, while the WV treatment results in a 24% capacity increase. The increase in capacity in Ar- and N<sub>2</sub>-treated samples can be explained by increased electrical conductivity due to oxygen vacancies. On the other hand, the improved electrochemical properties in WV-treated sample can be attributed to facilitated Li ion diffusion caused by Ti vacancies. The capacity increase due to Ti vacancy formation suggests that electrical conductivity may not be the most significant indicator as to whether battery

Table 3 Li diffusivities obtained from Warburg factors derived from EIS fitting

Atmosphere	Li diffusivity (cm <sup>2</sup> s <sup>-1</sup> )
O <sub>2</sub>	2.20 × 10 <sup>-13</sup>
Ar	2.32 × 10 <sup>-13</sup>
N <sub>2</sub>	4.30 × 10 <sup>-12</sup>
WV	1.04 × 10 <sup>-11</sup>



performance can be improved. Both electronic and ionic conductivity in intercalation oxide electrode materials need to be considered to understand their charge storage and transport properties.

## Conflicts of interest

There are no conflicts to declare.

## Acknowledgements

The authors acknowledge support from the National Science Foundation under Grant No. DMR-1408949. This work was also supported by the National Science Foundation *via* the Research Experience for Teachers: Materials for Society at Boise State University (DMR-1658076). The authors gratefully acknowledge fruitful discussions with Dr C. Chan and helpful suggestions from Drs B. Knowlton, R. Uvic and D. Tenne. The authors are thankful for the suggestions from Dr K. Swider-Lyons for the experimental setups on defect generation using water vapor treatment. We would also like to acknowledge Dr P. Davis for his help with the use of the Horiba Scientific LabRam HR Evolution Raman spectrometer.

## Notes and references

- D. Deng, M. G. Kim, J. Y. Lee and J. Cho, *Energy Environ. Sci.*, 2009, **2**, 818–837.
- K. Lee, A. Mazare and P. Schmuki, *Chem. Rev.*, 2014, **114**, 9385–9454.
- R. M. Gao, Z. Jiao, Y. Wang, L. Q. Xu, S. S. Xia and H. J. Zhang, *Chem. Eng. J.*, 2016, **304**, 156–164.
- M. Fehse and E. Ventosa, *ChemPlusChem*, 2015, **80**, 785–795.
- D. Bresser, B. Oschmann, M. N. Tahir, F. Mueller, I. Lieberwirth, W. Tremel, R. Zentel and S. Passerini, *J. Electrochem. Soc.*, 2015, **162**, A3013–A3020.
- Y. Li, J. D. Luo, X. Y. Hu, X. F. Wang, J. C. Liang and K. F. Yu, *J. Alloys Compd.*, 2015, **651**, 685–689.
- G. S. Zakharova, C. Jahne, A. Popa, C. Taschner, T. Gemming, A. Leonhardt, B. Buchner and R. Klingeler, *J. Phys. Chem. C*, 2012, **116**, 8714–8720.
- W. H. Ryu, D. H. Nam, Y. S. Ko, R. H. Kim and H. S. Kwon, *Electrochim. Acta*, 2012, **61**, 19–24.
- M. S. Li, X. F. Li, W. H. Li, X. B. Meng, Y. Yu and X. L. Sun, *Electrochem. Commun.*, 2015, **57**, 43–47.
- J. Kim and J. Cho, *J. Electrochem. Soc.*, 2007, **154**, A542–A546.
- S. K. Panda, Y. Yoon, H. S. Jung, W. S. Yoon and H. Shin, *J. Power Sources*, 2012, **204**, 162–167.
- L. L. Fan, X. F. Li, B. Yan, J. M. Feng, D. B. Xiong, D. J. Li, L. Gu, Y. R. Wen, S. Lawes and X. L. Sun, *Adv. Energy Mater.*, 2016, **6**, 1502057.
- T. Su, Y. L. Yang, Y. Na, R. Q. Fan, L. Li, L. G. Wei, B. Yang and W. W. Cao, *ACS Appl. Mater. Interfaces*, 2015, **7**, 3754–3763.
- G. M. Wang, Y. Yang, D. D. Han and Y. Li, *Nano Today*, 2017, **13**, 23–39.
- B. Koo, H. Xiong, M. D. Slater, V. B. Prakapenka, M. Baasubramanian, P. Podsiadlo, C. S. Johnson, T. Rajh and E. V. Shevchenko, *Nano Lett.*, 2012, **12**, 2429–2435.
- J. X. Qiu, S. Li, E. Gray, H. W. Liu, Q. F. Gu, C. H. Sun, C. Lai, H. J. Zhao and S. Q. Zhang, *J. Phys. Chem. C*, 2014, **118**, 8824–8830.
- D. W. Liu, P. Xiao, Y. H. Zhang, B. B. Garcia, Q. F. Zhang, Q. Guo, R. Champion and G. Z. Cao, *J. Phys. Chem. C*, 2008, **112**, 11175–11180.
- G. M. Wang, H. Y. Wang, Y. C. Ling, Y. C. Tang, X. Y. Yang, R. C. Fitzmorris, C. C. Wang, J. Z. Zhang and Y. Li, *Nano Lett.*, 2011, **11**, 3026–3033.
- A. Ghicov, H. Tsuchiya, J. M. Macak and P. Schmuki, *Phys. Status Solidi A*, 2006, **203**, R28–R30.
- R. S. Hyam, J. Lee, E. Cho, J. Khim and H. Lee, *J. Nanosci. Nanotechnol.*, 2012, **12**, 8908–8912.
- K. A. Smith, A. I. Savva, C. J. Deng, J. P. Wharry, S. Hwang, D. Su, Y. Q. Wang, J. Gong, T. Xu, D. P. Buttf and H. Xiong, *J. Mater. Chem. A*, 2017, **5**, 11815–11824.
- B. P. Uberuaga and X. M. Bai, *J. Phys.: Condens. Matter*, 2011, **23**, 435004.
- B. P. Hahn, J. W. Long, A. N. Mansour, K. A. Pettigrew, M. S. Osofsky and D. R. Rolison, *Energy Environ. Sci.*, 2011, **4**, 1495–1502.
- S. J. Liu, Q. Ma, F. Gao, S. H. Song and S. Gao, *J. Alloys Compd.*, 2012, **543**, 71–78.
- D. Xiong, X. Li, Z. Bai and S. Lu, *Small*, 2018, **14**, 1703419.
- A. Z. Liao, C. W. Wang, J. B. Chen, X. Q. Zhang, Y. Li and J. Wang, *Mater. Res. Bull.*, 2015, **70**, 988–994.
- X. H. Lu, G. M. Wang, T. Zhai, M. H. Yu, J. Y. Gan, Y. X. Tong and Y. Li, *Nano Lett.*, 2012, **12**, 1690–1696.
- L. X. Sang, Z. Y. Zhang and C. F. Ma, *Int. J. Hydrogen Energy*, 2011, **36**, 4732–4738.
- P. Xiao, D. W. Liu, B. B. Garcia, S. Sepelri, Y. H. Zhang and G. Z. Cao, *Sens. Actuators, B*, 2008, **134**, 367–372.
- M. Salari, K. Konstantinov and H. K. Liu, *J. Mater. Chem.*, 2011, **21**, 5128–5133.
- K. E. Swider-Lyons, C. T. Love and D. R. Rolison, *Solid State Ionics*, 2002, **152**, 99–104.
- H. Xiong, H. Yildirim, P. Podsiadlo, J. Zhang, V. B. Prakapenka, J. P. Greeley, E. V. Shevchenko, K. K. Zhuravlev, S. Tkachev, S. K. R. S. Sankaranarayanan and T. Rajh, *Phys. Rev. Lett.*, 2013, **110**, 078304.
- B. P. Hahn, J. W. Long and D. R. Rolison, *Acc. Chem. Res.*, 2013, **46**, 1181–1191.
- G. Kresse and J. Furthmuller, *Phys. Rev. B: Condens. Matter Mater. Phys.*, 1996, **54**, 11169–11186.
- J. P. Perdew, K. Burke and M. Ernzerhof, *Phys. Rev. Lett.*, 1996, **77**, 3865–3868.
- A. I. Liechtenstein, V. I. Anisimov and J. Zaanen, *Phys. Rev. B: Condens. Matter Mater. Phys.*, 1995, **52**, R5467–R5470.
- M. Landmann, E. Rauls and W. G. Schmidt, *J. Phys.: Condens. Matter*, 2012, **24**, 195503.
- Z. S. Lin, A. Orlov, R. M. Lambert and M. C. Payne, *J. Phys. Chem. B*, 2005, **109**, 20948–20952.

- 39 I. Nakamura, N. Negishi, S. Kutsuna, T. Ihara, S. Sugihara and E. Takeuchi, *J. Mol. Catal. A: Chem.*, 2000, **161**, 205–212.
- 40 S. N. Phattalung, S. Limpijumnong and J. Yu, *Appl. Catal., B*, 2017, **200**, 1–9.
- 41 S. Livraghi, M. C. Paganini, E. Giamello, A. Selloni, C. Di Valentin and G. Pacchioni, *J. Am. Chem. Soc.*, 2006, **128**, 15666–15671.
- 42 F. Dong, W. R. Zhao, Z. B. Wu and S. Guo, *J. Hazard. Mater.*, 2009, **162**, 763–770.
- 43 R. Sanjines, H. Tang, H. Berger, F. Gozzo, G. Margaritondo and F. Levy, *J. Appl. Phys.*, 1994, **75**, 2945–2951.
- 44 B. Roh, PhD thesis, The Pennsylvania State University, 2007.
- 45 N. Baram and Y. Ein-Eli, *J. Phys. Chem. C*, 2010, **114**, 9781–9790.
- 46 H. Tang, K. Prasad, R. Sanjines, P. E. Schmid and F. Levy, *J. Appl. Phys.*, 1994, **75**, 2042–2047.
- 47 I. Hanzu, T. Djenizian and P. Knauth, *J. Phys. Chem. C*, 2011, **115**, 5989–5996.
- 48 S. Z. Islam, A. Reed, N. Wanninayake, D. Y. Kim and S. E. Rankin, *J. Phys. Chem. C*, 2016, **120**, 14069–14081.
- 49 L. K. Tsui and G. Zangari, *Electrochim. Acta*, 2014, **121**, 203–209.
- 50 V. K. Mahajan, M. Misra, K. S. Raja and S. K. Mohapatra, *J. Phys. D: Appl. Phys.*, 2008, **41**, 125307.
- 51 A. Tighineanu, T. Ruff, S. Albu, R. Hahn and P. Schmuki, *Chem. Phys. Lett.*, 2010, **494**, 260–263.
- 52 R. A. Spurr and H. Myers, *Anal. Chem.*, 1957, **29**, 760–762.
- 53 O. K. Varghese, D. W. Gong, M. Paulose, C. A. Grimes and E. C. Dickey, *J. Mater. Res.*, 2003, **18**, 156–165.
- 54 M. D. Earle, *Phys. Rev.*, 1942, **61**, 56–62.
- 55 T. Ohsaka, F. Izumi and Y. Fujiki, *J. Raman Spectrosc.*, 1978, **7**, 321–324.
- 56 D. Georgescu, L. Baia, O. Ersen, M. Baia and S. Simon, *J. Raman Spectrosc.*, 2012, **43**, 876–883.
- 57 S. Sahoo, A. K. Arora and V. Sridharan, *J. Phys. Chem. C*, 2009, **113**, 16927–16933.
- 58 V. Swamy, A. Kuznetsov, L. S. Dubrovinsky, R. A. Caruso, D. G. Shchukin and B. C. Muddle, *Phys. Rev. B: Condens. Matter Mater. Phys.*, 2005, **71**, 184302.
- 59 J. C. Parker and R. W. Siegel, *J. Mater. Res.*, 1990, **5**, 1246–1252.
- 60 J. C. Parker and R. W. Siegel, *Appl. Phys. Lett.*, 1990, **57**, 943–945.
- 61 M. J. Scepanovic, M. U. Grujic-Brojcin, Z. D. Dohcevic-Mitrovic and Z. V. Popovic, *Mater. Sci. Forum*, 2006, **518**, 101–106.
- 62 P. Scherrer, *Nachr. Ges. Wiss. Goettingen, Math.-Phys. Kl.*, 1918, **2**, 98–100.
- 63 J. G. Wang, P. Zhang, X. Li, J. Zhu and H. X. Li, *Appl. Catal., B*, 2013, **134**, 198–204.
- 64 J. W. Xu, C. H. Jia, B. Cao and W. F. Zhang, *Electrochim. Acta*, 2007, **52**, 8044–8047.
- 65 K. Zhu, Q. Wang, J. H. Kim, A. A. Pesaran and A. J. Frank, *J. Phys. Chem. C*, 2012, **116**, 11895–11899.
- 66 H. T. Fang, M. Liu, D. W. Wang, T. Sun, D. S. Guan, F. Li, J. G. Zhou, T. K. Sham and H. M. Cheng, *Nanotechnology*, 2009, **20**, 225701.
- 67 H. Han, T. Song, E. K. Lee, A. Devadoss, Y. Jeon, J. Ha, Y. C. Chung, Y. M. Choi, Y. G. Jung and U. Paik, *ACS Nano*, 2012, **6**, 8308–8315.
- 68 U. Lafont, D. Carta, G. Mountjoy, A. V. Chadwick and E. M. Kelder, *J. Phys. Chem. C*, 2010, **114**, 1372–1378.
- 69 D. Bresser, E. Paillard, E. Binetti, S. Krueger, M. Striccoli, M. Winter and S. Passerini, *J. Power Sources*, 2012, **206**, 301–309.
- 70 A. Moretti, G. T. Kim, D. Bresser, K. Renger, E. Paillard, R. Marassi, M. Winter and S. Passerini, *J. Power Sources*, 2013, **221**, 419–426.
- 71 J. X. Duan, H. Y. Hou, X. X. Liu, C. X. Yan, S. Liu, R. J. Meng, Z. L. Hao, Y. Yao and Q. S. Liao, *J. Porous Mater.*, 2016, **23**, 837–843.
- 72 A. Auer, E. Portenkirchner, T. Gotsch, C. Valero-Vidal, S. Penner and J. Kunze-Liebhauser, *ACS Appl. Mater. Interfaces*, 2017, **9**, 36828–36836.
- 73 M. Bratic, D. Jugovic, M. Mitric and N. Cvjeticanin, *J. Alloys Compd.*, 2017, **712**, 90–96.
- 74 D. Aurbach, M. D. Levi, E. Levi, H. Teller, B. Markovsky, G. Salitra, U. Heider and L. Heider, *J. Electrochem. Soc.*, 1998, **145**, 3024–3034.